High-Resolution X-ray Structure of Gln143Asn Manganese Superoxide Dismutase Captures Multiple Hydrogen Peroxide Binding Sites

Medhanjali Dasgupta,[a] Katelyn Slobodnik,[a] Erika A. Cone,[a] Jahaun Azadmanesh,[a] Thomas Kroll[b] and Gloria E.O. Borgstahl[a*]

[a] Eppley Institute for Research in Cancer and Allied Diseases, University of Nebraska Medical Center, Omaha, NE, 68198, USA

[b] Stanford Synchrotron Radiation Lightsource, SLAC National Accelerator Laboratory, Menlo Park, CA, 94025, USA

[*]Correspondence email: gborgstahl@unmc.edu

Synopsis A high-resolution X-ray structure of a Gln143Asn variant of manganese superoxide dismutase reveals multiple hydrogen peroxide binding sites beyond the canonical LIG and PEO binding positions within the active site. These findings expand the known landscape of product peroxide-bound states in MnSOD.

Abstract Human mitochondrial manganese superoxide dismutase (MnSOD) converts superoxide ($O_2^{\bullet-}$) into hydrogen peroxide (H_2O_2) and molecular oxygen (O_2), serving as a key defense against oxidative damage. Despite extensive studies, the full structural characterization of H_2O_2-binding sites in MnSOD remains largely unexplored. Previous H_2O_2-soaked MnSOD structures have identified two distinct H_2O_2-binding sites: one directly ligated to the catalytic Mn (LIG position) and another at the active site gateway (PEO position) between second-shell residues Tyr34 and His30. In this study, a kinetically impaired Gln143Asn MnSOD variant is used to trap and explore additional H_2O_2-binding sites beyond the second-shell solvent gate. In the wild-type enzyme, Gln143 mediates proton transfers with the Mn-bound solvent (WAT1) to drive redox cycling of the metal, necessary for effective $O_2^{\bullet-}$ dismutation. Substitution with Asn stalls catalysis because the increased distance from WAT1 disrupts critical proton-coupled electron transfer (PCET) events, and the redox cycling of the active site metal is impaired. This, in turn, stalls the electrostatic cycling of positive charge on the enzyme surface and enhances the likelihood of trapping transient H_2O_2-bound states in this variant. Results reveal several H_2O_2 molecules leading up to the active site, in addition to the canonical LIG and PEO positions.

Keywords: **Manganese superoxide dismutase; Peroxide binding; Metalloenzyme; X-ray crystallography.**

1. Introduction

Human manganese superoxide dismutase (MnSOD) is a mitochondrial matrix metalloenzyme that catalyzes the dismutation of reactive superoxide radicals ($O_2^{\bullet-}$), generated as by-products of mitochondrial respiration, into molecular oxygen (O_2) and hydrogen peroxide (H_2O_2) (Abreu & Cabelli, 2010). As the only known mitochondrial enzyme capable of converting reactive $O_2^{\bullet-}$ radicals into diffusible products that can be further metabolized or exported, MnSOD serves as the critical first line of defense against oxidative stress (Bresciani *et al.*, 2015, Grujicic & Allen, 2025). Unsurprisingly, dysregulation of MnSOD activity is associated with various human diseases, highlighting the continued need for a detailed structural understanding of its catalytic mechanism.

Human MnSOD physiologically functions as a homotetramer, with each active site containing a Mn ion, which cycles between oxidized (trivalent, Mn^{3+}, pink) and reduced (divalent, Mn^{2+}, colorless) states to drive two half-reactions to complete the catalytic cycle (Borgstahl *et al.*, 1992, Fee & Bull, 1986, Hsu *et al.*, 1996).

$$Mn^{3+}\text{-WAT1}(OH^-) + O_2^{\bullet-} \leftrightarrow Mn^{2+}\text{-WAT1}(H_2O) + O_2 \quad (1)$$

$$Mn^{2+}\text{-WAT1}(H_2O) + O_2^{\bullet-} + 2H^+ \leftrightarrow Mn^{3+}\text{-WAT1}(OH^-) + H_2O_2 + O_2 \quad (2)$$

In the first half-reaction (Eq. 1), resting-state Mn^{3+} oxidizes $O_2^{\bullet-}$ to the first reaction product, O_2, which diffuses out of the mitochondria or gets reabsorbed into the mitochondrial electron transport chain. During this half reaction, the active site Mn is simultaneously reduced, and its WAT1 ligand receives a proton and becomes a water molecule (Azadmanesh *et al.*, 2021). In the second half-reaction (Eq. 2), Mn^{2+} binds a second $O_2^{\bullet-}$ radical, again protons and electrons are transferred simultaneously to form (H_2O_2 and to redox cycle the active site Mn. In this way, both half reactions use proton-coupled electron transfer (PCET) events (Reece & Nocera, 2009), to rapidly convert $O_2^{\bullet-}$ to O_2 and H_2O_2.

Decades of extensive structural characterization efforts have yielded 39 total human MnSOD structures in the Protein Data Bank (PDB). Out of them, almost all reported H_2O_2-soaked MnSOD structures have consistently identified H_2O_2 bound to the catalytic Mn, in a near side-on configuration, that replaces the WAT1 solvent (Azadmanesh *et al.*, 2025, Azadmanesh *et al.*, 2024, Porta *et al.*, 2010). This metal-ligated H_2O_2 binding site is typically referred to as the LIG position. A recent H_2O_2-soaked Trp161Phe MnSOD neutron structure identified a second H_2O_2 binding site, named PEO, between the second-shell gateway residues, Tyr34 and His30, at the opening of the active site solvent funnel (Azadmanesh *et al.*, 2025). While these structures offer valuable insights into active site H_2O_2 binding modes in MnSOD, to date, no electron density for H_2O_2 has been observed beyond the PEO binding site, on the solvent-exposed side of the active site funnel. This absence of any observable H_2O_2 binding beyond the MnSOD solvent gate, even in severely product-inhibited variants

such as Trp161Phe and Tyr34Phe MnSODs, suggests that once H□O□ crosses the Tyr34-His30 gateway, it rapidly escapes into bulk solvent.

Further complicating structural efforts, partially occupied or mobile H_2O_2 molecules are often indistinguishable from water (H_2O) in medium- to low-resolution X-ray maps, particularly in the absence of neutron diffraction data that can accurately resolve hydrogen positions. Thus, key questions remain unresolved: (i) What is the fate of H_2O_2 following release from the PEO site? (ii) Are there any transient H_2O_2 binding interactions occurring beyond the Tyr34-His30 solvent gateway? (iii) What governs H_2O_2 diffusion on the solvent-exposed surface of MnSOD? These questions are important because MnSOD catalysis is limited not by the chemical transformation itself, but by diffusion of substrate and product through the ~10 Å deep, ~5 Å wide active solvent cavity (Azadmanesh *et al.*, 2017).

The goal of this current study is to identify all possible H_2O_2 binding sites on the solvent-exposed side of the MnSOD solvent funnel, by using a kinetically slow and catalytically impaired Gln143Asn MnSOD variant (Hsieh *et al.*, 1998). Gln143 is a second sphere residue that plays a critical role in the PCET reaction mechanism of native MnSODs (Azadmanesh *et al.*, 2021). Azadmanesh and coworkers showed that in the first half-reaction, upon chemical reduction of Mn^{3+} to Mn^{2+}, Gln143 donates a proton to the active site metal-bound solvent (WAT1-OH^-) to generate WAT1-H_2O (Eq. 1). The WAT1-OH^- negative charge is thought to have stabilized the positive charge of Mn^{3+} in the oxidized state. Presumably, in the second half of the reaction (Eq. 2), Gln143 takes the proton back from WAT1-H_2O, regenerating the WAT1-OH^- negative charge simultaneously as Mn^{2+} is oxidized to Mn^{3+}. Through this critical and reversible proton transfer event, Gln143 is directly coupled to the redox cycling of the catalytic metal in MnSOD that drives its catalysis (Azadmanesh *et al.*, 2021). Substituting Gln143 with Asn preserves the active site architecture, but the hole created disrupts proton transfers with the WAT1 solvent. Consequently, redox cycling of the catalytic Mn is slowed, as evidenced by over 100-fold reductions in the corresponding kinetic rate constants, k_2 and k_4, relative to the wild-type MnSOD (Hsieh *et al.*, 1998) (Fig. 1). The kinetic rate constants of Gln143Asn MnSOD have the overall effect of tending to keep the active site Mn reduced. This significantly impairs Gln143Asn MnSOD catalytic turnover with a ~13-fold decrease in k_{CAT} value relative to wild-type MnSOD (wild-type k_{CAT} = 40 ms^{-1}, Gln143Asn k_{CAT} = 0.3 ms^{-1}). While this loss of catalytic efficiency compromises the overall function of Gln143Asn MnSOD, it offers a distinct experimental advantage for our study; the slowed turnover rate allows for greater control of experimental design, cryo-trapping, and structural characterization of H_2O_2 molecules bound. Our results reveal many H_2O_2 molecules beyond the canonical LIG and PEO positions, spanning the space extending from the edge of the Tyr34-His30 solvent gateway to the bulk solvent. These findings expand the structural landscape of how H_2O_2 exits the MnSOD active site.

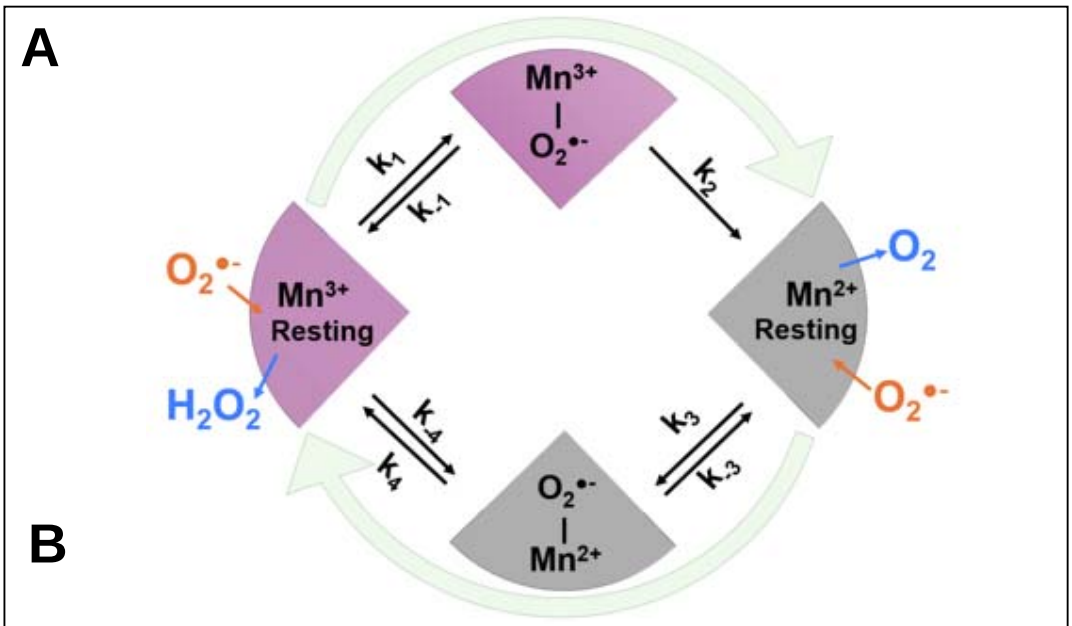

Equation	Rate constant	Gln143Asn MnSOD	Wildtype MnSOD
(1) $Mn^{3+} + O_2^{\bullet-} \leftrightarrow Mn^{2+} + O_2$	k_1 ($M^{-1}s^{-1}$)	2.0×10^9	2.0×10^9
	k_{-1} (s^{-1})	1.5×10^6	2.0×10^4
	k_2 (s^{-1})	600	8×10^4
(2) $Mn^{2+} + O_2^{\bullet-} + 2H^+ \leftrightarrow Mn^{3+} + H_2O_2$	k_3 ($M^{-1}s^{-1}$)	2.0×10^9	2.0×10^9
	k_{-3}(s^{-1})	1.5×10^6	2.0×10^4
	k_4 (s^{-1})	600	8×10^4
	k_{-4} ($M^{-1}s^{-1}$)	1×10^3	3×10^2

Figure 1 The kinetics of MnSOD catalysis. **(A)** MnSOD reaction scheme, **(B)** Kinetic parameters of human wild-type and Gln143Asn MnSOD enzymes. Data are from (Hsieh *et al.*, 1998).

2. Materials and Methods

2.1 Expression, purification, & crystallization of Gln143Asn MnSOD.

The Gln143Asn plasmid was ordered from GenScript and codon optimized for expression in *Escherichia coli. (E. coli)*. Following transformation of *E. coli* BL21(DE3) cells with the plasmid, a small culture was incubated at 37 °C and 225 rpm until visible turbidity was reached in Terrific Broth (TB) supplemented with 30 µg/L of kanamycin. Next, 2 L of TB supplemented with 30 µg/L of kanamycin and 16 mL of 100% glycerol was inoculated with ~5 mL of the small growth and incubated at 37 °C with vigorous shaking at 225 rpm until an OD_{600} of 0.8-1.0 was reached. A bolus of 8 mM $MnCl_2$ and 1 mM isopropyl β-d-1-thiogalactopyranoside (IPTG) was then added, and the flasks were incubated at 37 °C and 140 rpm overnight. Induced cells were harvested by centrifugation

using a Sorval Lynx 6000 with a Fiber Light F9-6x-1000 LEX rotor, operated at 4 °C and 8000 rpm for 40 minutes. The pellets were stored at –20 °C. For Gln143Asn MnSOD protein purification, pellets were thawed at room temperature and thoroughly resuspended in Lysis buffer (10 mM $MnCl_2$ and 10 mM MOPS pH 7.8), followed by filtration and removal of the insoluble fraction. Next, the soluble fraction was lysed with an EmulsiFlex-C3 at a pressure equal to or greater than 20,000 psi for ~5 sample passes. The lysate was centrifuged at 4 °C and 8,000 rpm for 40 minutes, and the supernatant was transferred to a hot water bath at 55 °C for 1 hour. Then, the solute was centrifuged again, and the supernatant (containing the soluble proteins) was diluted using 25 mM MES pH 5.5 at a 1:2 protein to buffer ratio. The diluted protein was then loaded onto a HiPrep 16x10 CMFF cation exchange column using an ÄKTA Pure HPLC (GE Healthcare). The sample was buffer exchanged into 10 mM MES at pH 5.5 on the column, followed by protein elution from the resin with 10 mM MES at pH 6.5. Purification was confirmed by the presence of a single band corresponding to the correct molecular weight of 23 kDa on a 4-12% SDS PAGE gel stained with Coomassie blue. Before crystallization, all pure fractions were pooled together, and buffer exchanged into 0.25 mM potassium phosphate (pH 7.8) using a 10 kDa concentrator (Millipore, Sigma Aldrich) and concentrated to ~23 mg/ml (~1 mM).

Twenty-four well hanging drop trays were set up with a 1:1 ratio of concentrated protein against reservoir solution containing 1.8 M potassium phosphate (pH 7.8) and incubated at room temperature. Gln143Asn MnSOD crystallized in the high-symmetry space group of $P6_122$, and the crystals grew to final sizes of ~ 100 µm long in a week. The crystal trays were hand-carried by flight to the Stanford Synchrotron Radiation Lightsource (SSRL) for data collection.

2.2 X-ray crystallography data collection, processing, refinement, & validation.

A single crystal of Gln143Asn MnSOD was exchanged into cryo-solution (2.5 M potassium phosphate, pH 7.8) at room temperature, manually plunged into liquid nitrogen, then mounted with a 100 µm-sized cryo-loop (MiTeGen) at SSRL beamline 14-1. The mounted crystal was annealed by manually blocking the cryo-stream for 5 seconds. For H_2O_2 soaking, a 30% stock solution of H_2O_2 (Millipore Sigma) was diluted 100x and pipetted into the drop of mother liquor containing the single Gln143Asn crystal, to reach a final H_2O_2 concentration of 0.3% *in-crystallo*. The total soaking time was ~30 seconds at room temperature, followed by quick plunging into liquid nitrogen to cryo-trap the soaked H_2O_2 in the crystal, mounting, and annealing like the resting-state, resting state Gln143Asn MnSOD crystal. The process is schematized in Supplementary Information Fig. S1. X-ray crystallography data for both the resting-state and H_2O_2-treated Gln143Asnwere collected at 100 K, using a Dectris Pilatus 16M PAD detector and a controllable axial nitrogen cryo-stream (Oxford Cryosystems, Ltd.). Data collection parameters are summarized in Supplementary Information Table S1. Initial phases were obtained using the Phaser Molecular Replacement (Phaser-MR) package within the Phenix software suite with the wild-type MnSOD structure (PDB ID 7KLB) (Azadmanesh

et al., 2021)serving as the phasing model. Model building was performed with COOT followed by iterative rounds of refinement cycles using Phenix_refine**.** All refinement strategies were based on maximum likelihood-based target functions and included the refinement of i) individual atomic coordinates (in both reciprocal and real space), and ii) individual isotropic atomic displacement parameters (ADPs) for all atoms, with automatic weight optimisation. Only riding hydrogens were added to the models (Liebschner, 2020) and appropriate metal coordination restraints were generated using idealised geometries, with the ReadySet tool. Gln143Asn, like the wild-type enzyme, crystallizes as a homodimer, with monomers A and B in the asymmetric unit, and crystallographic symmetry operations were applied to generate the physiological tetramer, using the PyMOL Molecular Graphics System (Schrodinger, LLC). Final model validations were performed using MolProbity. Coordinate error estimates, calculated with Phenix_refine, are reported Supplementary Information Table S1 as a measure of model precision. Coordinates and structure factors for the resting-state and H_2O_2-treated Gln143Asn MnSOD X-ray crystal structures have been deposited in the Protein Data Bank (PDB) under accession codes 9NR0 and 9NSJ, respectively.

2.3 Metal center specific electrostatic surface generation.

To generate the solvent-excluded electrostatic surfaces of tetrameric MnSOD proteins that accurately reflect the electronic charge distribution, spin multiplicity, and redox potential of the active site Mn centers, we implemented a three-step protocol to account for electronic effects imparted by its primary coordination sphere (PCS) ligands (Van Stappen *et al.*, 2022), schematized in Supplementary Information Fig. S2.

Step 1. Initial per-residue charges were assigned using the PDB2PQR (Dolinsky *et al.*, 2007) web service, hosted at poissonboltzmann.org. This generated PQR files containing i) atomic partial charges of all residues, computed using the AMBER force field (Hornak *et al.*, 2006) and ii) protonation states of ionizable residues, based on pKa values predicted by PROPKA 3.0 at pH 7.0 (Olsson *et al.*, 2011).

Step 2. To determine the electronic properties of the catalytic Mn in specific redox and spin states, the protein structures were truncated to only retain the first-shell ligands coordinating the Mn ion, thereby preserving the key geometric and electronic features of the metal site. Density functional theory (DFT) calculations were performed on the isolated metal centers, using the high-spin sextet state for the divalent Mn ion in Gln143Asn enzyme (Azadmanesh *et al.*, 2025), according to established protocols in (Neves *et al.*, 2013, Azadmanesh *et al.*, 2017). Single-atomic electrostatic potential (ESP) charges for the Mn ion and its direct ligands were derived using the Merz-Kollman scheme and subsequently refined using the restrained electrostatic potential (RESP) methodology. As a benchmark, we applied the same DFT protocol to the five-coordinate, high-spin quintet resting-state of the wild-type Mn^{3+}SOD enzyme (PDB ID 5VF9) (Azadmanesh *et al.*, 2017). All DFT-calculated ESP charges are given in Fig. 4C.

Step 3. The ESP-refined metal charges were then integrated with the remainder of the tetrameric protein's PQR-derived charges to compute full electrostatic surface maps using the Adaptive Poisson-Boltzmann Solver (APBS) Electrostatics plugin within PyMOL, following the established protocol in (Azadmanesh *et al.*, 2017).

2.4 Mn K-edge HERFD XANES spectroscopy data collection, processing, & analysis.

A solution of 3 mM Gln143Asn MnSOD (~70 mg ml^{-1}) in 25 mM potassium phosphate (pH 7.8) was treated with 280 mM (1% *w/v*) H_2O_2 to isolate the H_2O_2-bound state of the Gln143Asn variant. Mn K-edge HERFD-XANES spectra (Proux *et al.*, 2017) were recorded using a liquid He cryostat at 10 K, at beamline 15 -2 of SSRL. The incident energy was tuned to the first derivative of an internal Mn foil at 6539 eV. X-ray irradiation was carefully monitored so that two subsequent scans of the same spot did not have photoreduction differences, and different spots along samples were scanned. When appropriate, aluminium foil was inserted into the beam path to attenuate the incident flux. For HERFD-XANES measurements, a Johann-type hard X-ray spectrometer with six Mn analyser crystals were used with a liquid-nitrogen cooled Si (311) double crystal monochromator. Experimental spectra were processed, visualized, and plotted using the Larch software package. The post-edge regions were normalized, and pre-edge peak fittings were done using pseudo-Voigt functions. Pre-edge intensities were quantified as the integrated area under the fitted curves.

3.1 Multiple H_2O_2 binding sites were revealed beyond the Tyr34-His30 solvent gateway in Gln143Asn MnSOD.

In this present study, we report two high-resolution X-ray crystal structures of the Gln143Asn MnSOD enzyme: (i) a 1.33 Å structure of H_2O_2-treated (PDB ID: 2NR0) and (ii) a 1.55 Å structure of the untreated resting-state (PDB ID: 2NSJ). Superposition of these two structures reveals that H_2O_2 soaking and cryotrapping triggers a striking accumulation of at least five distinct H_2O_2 molecules, either fully, or partially occupying the space between the solvent-exposed enzyme surface and the Tyr34-His30 solvent gate in Gln143Asn MnSOD (Fig. 2A). These H_2O_2 molecules in the bulk solvent are named L_b for Lig_{bulk}. We compared L_b H_2O_2 (Fig. 2A,C, red sticks) to the corresponding water positions in the resting-state structure (Fig. 2D). Superposition shows that one or both oxygen atoms of the L_b H_2O_2 overlap with either fully or partially occupied water molecules in the untreated resting-state structure (Fig. 2D, blue spheres), indicating that the H_2O_2 molecules are hydrogen bonding to similar residues on the surface.

The L_b H_2O_2 molecules bind to the solvent-exposed surface of the Gln143Asn MnSOD tetramer (Fig. 2A,B). We note that the resting state electrostatic solvent accessible surface of Gln143Asn MnSOD is different than the surface of resting state wild-type MnSOD. The active site funnel of wild-type is much more positively charged than Gln143Asn. This is because the wild-type resting state is Mn^{3+}, and the Gln143Asn resting state is Mn^{2+}. The surface of wild-type MnSOD in the reduced state is

practically identical to that of Gln143Asn. When wild-type MnSOD cycles its redox state during catalysis, its electrostatic surface cycles between the positive and more neutral surfaces. Gln143Asn will stay in the more neutral surface most of the time and this seems to help stabilize the H_2O_2 binding

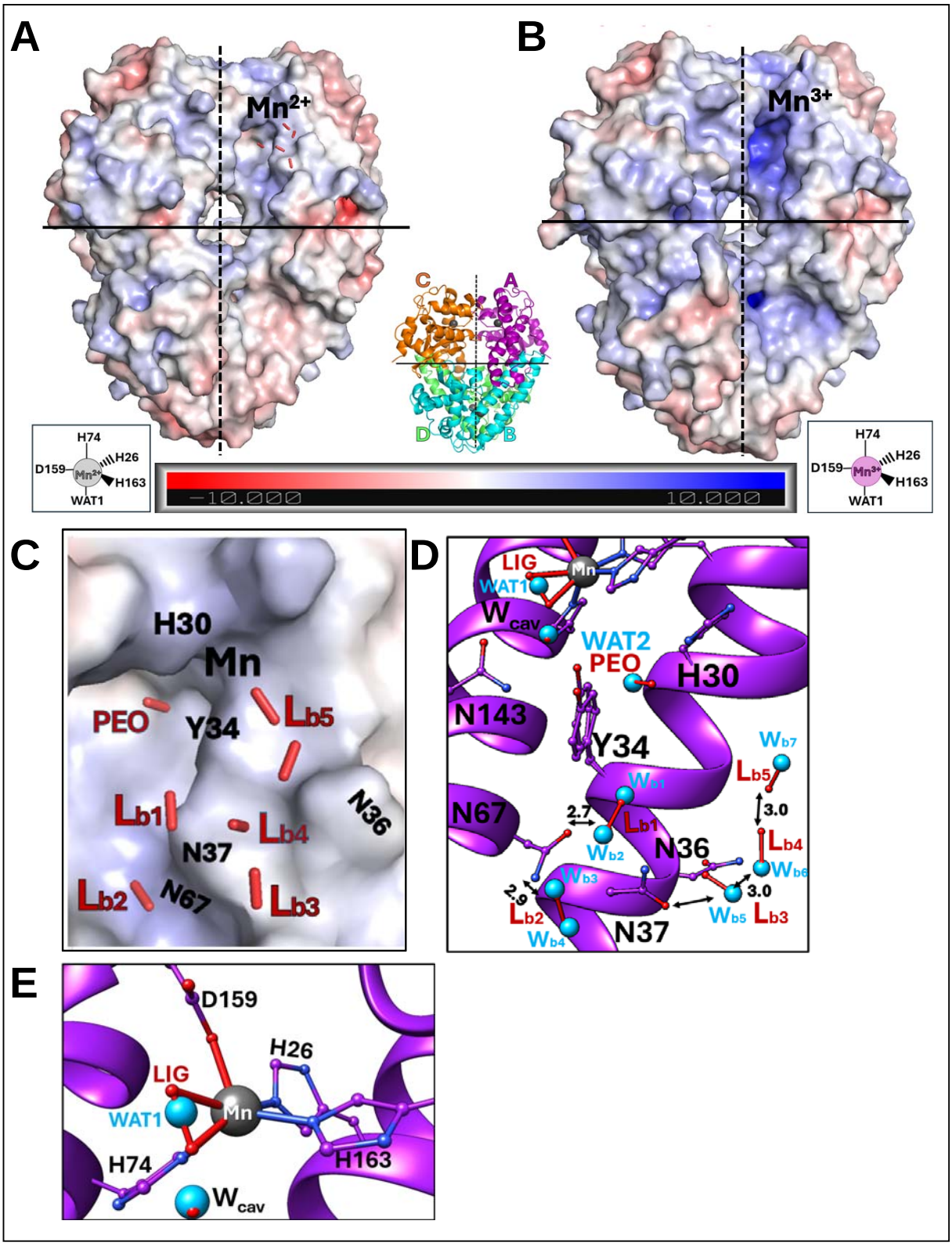

sites.

Figure 2 H_2O_2 binding. **(A-B)** Resting state Gln143Asn and wild-type MnSOD enzymes, overlaid on their respective electrostatic surfaces, with the location of the chain A active site Mn labelled. All bulk-exposed L_b peroxides trapped in the Gln143Asn enzyme are shown as red sticks. Dimeric and tetrameric interfaces are marked by dashed and solid black lines, respectively. Insets show the penta-valent Mn^{2+} (grey sphere) and Mn^{3+} (pink sphere) ions and their primary coordination sphere ligands in the Gln143Asn and wild-type enzymes, respectively. The middle inset shows the ribbon diagram of the tetrameric Gln143Asn MnSOD, with Mn ions shown as grey spheres. **(C)** Zoomed-in view of L_b H_2O_2 (red sticks), on top of the displayed electrostatic surface. **(D)** All modelled H_2O_2, active site (top), and the Tyr34-His30 solvent gate with the resting state water molecules (blue spheres). **(E)** Zoomed-in view of the active site of Gln143Asn, with bound LIG (red stick) peroxide in the treated structure, and the WAT1 solvent (blue sphere) and Wcav.

To validate that the L_b electron densities observed in the H_2O_2-treated structure truly correspond to H_2O_2 molecules, rather than misassigned or mobile waters, we modeled fully occupied water (copied from the resting-state position) at each L_b site and studied the electron density after refinement. This analysis shows that each H_2O_2 site has an elongated 2Fo-Fc density. When modelled with a water molecule in trial refinements, the density is not satisfied, and residual Fo-Fc density remains (Supporting Information Fig. S3). This analysis confirms the identification of H_2O_2 binding sites. This many H_2O_2 molecules have never been observed in any previous MnSOD structure, and provide strong validation for our chosen experimental strategy, which leverages the slowed catalysis of the Gln143Asn variant to reveal all potential H_2O_2 binding sites in MnSOD.

In addition to the L_b H_2O_2 molecules on the solvent-exposed surface, we observe H_2O_2 binding at the metal-ligated LIG position, and at the PEO position at the mouth of the active site solvent-funnel gateway in between second-shell residues Tyr34 and His30. Overall, H_2O_2 treatment does not appear to significantly alter the active site architecture of Gln143Asn MnSOD, except for the partial displacement of the Mn-bound solvent (WAT1) by a partially occupied (~35%) H_2O_2 molecule bound at the LIG position, opposite His26 (Fig. 2E). Superposition with all other previously published structures of H_2O_2-treated human MnSODs, i.e. wild-type (PDB ID 8VJ5) (Fig. 3A,B yellow), Trp161Phe (Fig. 3C cyan), and Tyr34Phe (Fig. 3C red), as well as *E.coli* wild-type MnSODs (PDB ID 3K9S) (Fig. 3A,B orange) shows that H_2O_2 binds the active site LIG position in the Gln143Asn variant (Fig. 3A-C, purple) in a configuration very similar to the previously observed nearly side-on binding modes in the human MnSOD variants, rather than end-on, as seen in the *E.coli* wild-type MnSOD.

Additionally, we observe a 57% occupied H_2O_2 near the PEO binding site, which has so far only

been observed in the H_2O_2-soaked neutron structure of Trp161Phe MnSOD (PDB ID 8VHW) (Azadmanesh *et al.*, 2024), at full occupancy (Fig. 3C cyan). Superposition of the two H_2O_2-bound

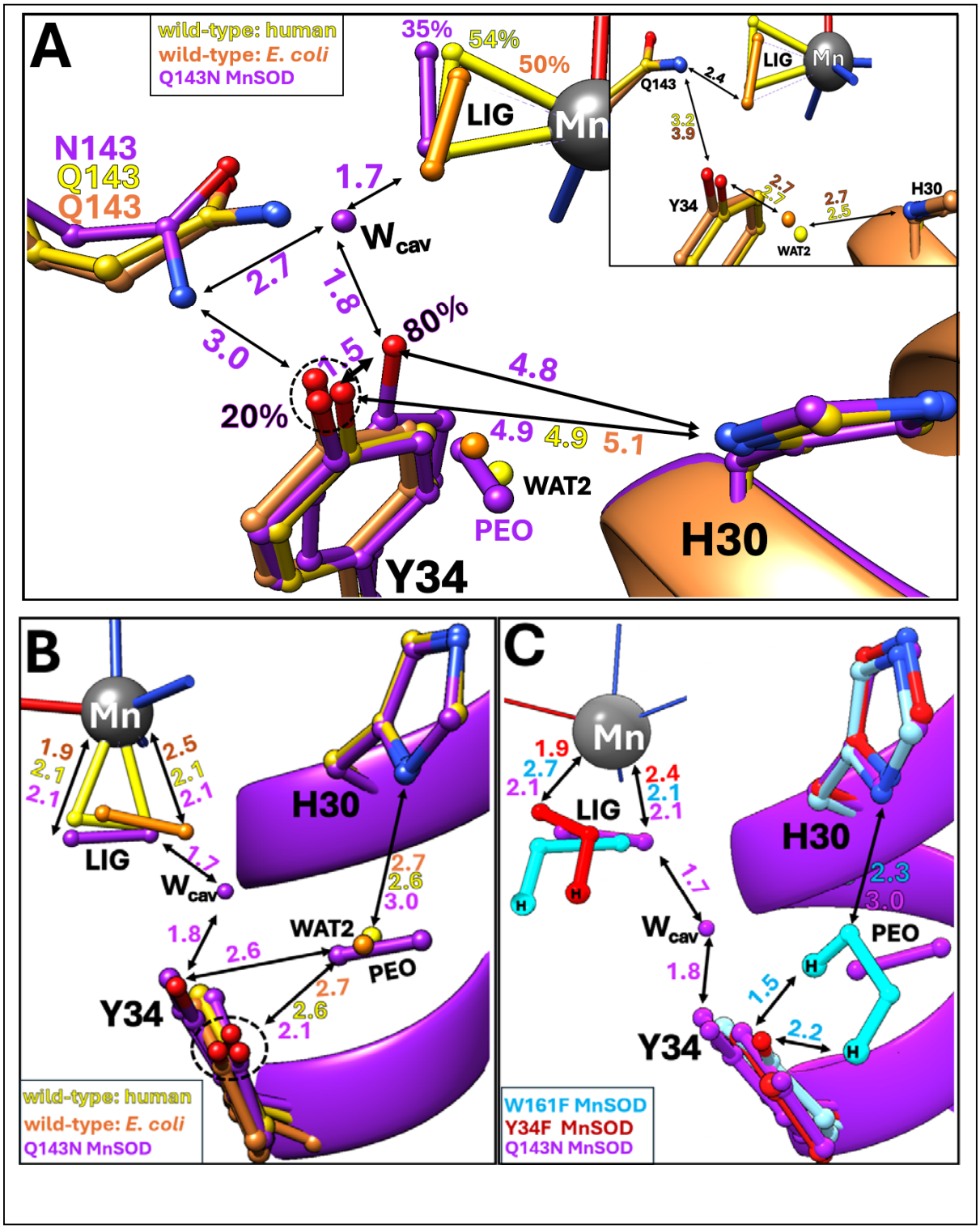

MnSOD structures reveals that H_2O_2 binds at the PEO site of the Gln143Asn variant (Fig. 3C, purple) at a slightly different configuration. However, we do not know what causes this change in H_2O_2 binding at the PEO site of Gln143Asn MnSOD.

Figure 3 Comparison with known H_2O_2 soaked MnSOD in the PDB. Structural comparisons of H_2O_2 -treated human Gln143Asn MnSOD (purple) with (**A,B)** both human (yellow, PDB ID 8VJ5), and *E. coli* (orange, PDB ID 3K9S) wild-type enzymes, respectively, as well as with **(C)** the product inhibited MnSOD variants, Trp161Phe (cyan, neutron PDB ID 8VHW) and Tyr34Phe (red, neutron PDB ID 9BVY). We observe H_2O_2 binding in the pre-established LIG and PEO binding sites, with subtle differences, potentially owing to the Gln143 mutation-induced cavity. Notably, Tyr34 samples a shifted conformation (~80% occupancy) in this cavity, drawing closer to both the LIG H_2O_2 and His30. This conformational flexibility is not typically observed in wild-type or other variants lacking this mutation-induced cavity, between the metal primary sphere and the second-shell solvent gateway.

3.2 Peroxide binding subtly alters the active site electrostatics Gln143Asn MnSOD without changing the redox or coordination states of the catalytic Mn.

To monitor changes in the oxidation state and coordination geometry of the catalytic Mn in the Gln143Asn variant upon H_2O_2 treatment, we compared the Mn K-edge High-Energy-Resonance Fluorescence-Detected X-ray Absorption Near-Edge Spectra (HERFD-XANES) of the purified enzyme, before and after H_2O_2 treatment, following protocols established in (Azadmanesh *et al.*, 2025, Azadmanesh *et al.*, 2024). We observe no detectable shift in either rising edge or pre-edge features (Fig. 4A blue vs red), indicating no alteration in the redox state or coordination geometry of the catalytic Mn after H_2O_2 treatment in Gln143Asn MnSOD. Notably, the spectral features of both Gln143Asn samples closely resemble those of the H_2O_2-treated wild-type MnSOD (Fig. 4A yellow), which has been previously established to contain the reduced Mn^{2+} ion in its active site (Azadmanesh *et al.*, 2024). The pre-edge intensities of both Gln143Asn samples are comparable to each other and the H_2O_2-treated wild-type enzyme, indicating highly similar metal centers across all three conditions. In contrast, the spectrum of the resting-state wild-type MnSOD (Fig. 4A, black) shows a clear shift of both rising and pre-edge features toward higher energies, consistent with the established presence of an oxidized Mn^{3+} metal in the resting wild-type MnSOD.

DFT calculations predict no significant change in the charge or spin state of the catalytic Mn^{2+} in Gln143Asn enzyme, upon H_2O_2 treatment. However, certain trends emerge (Fig. 4BC): (i) Charges of both His26, and His74 switch signs, going from positive to negative (and closer to the wild-type resting-state values), (ii) Asp159 is less negatively charged in the resting-state of Gln143Asn, compared to wild-type, but becomes more negative, with H_2O_2 addition, and (iii) His163 flips from negative to positive charge when comparing the wild-type to the variant, indicating potential protonation state change. However, these conclusions remain to be experimentally validated. Moreover, it is important to note that our DFT models treat LIG as a di-oxygen species rather than H_2O_2, to account for the caveat that X-ray electron density maps cannot pinpoint proton positions accurately. This is particularly relevant considering recent neutron diffraction studies of H_2O_2-soaked Trp161Phe (Fig. 3C cyan), and Tyr34Phe (Fig. 3C red) Mn^{2+}SODs, both of which stabilize a singly

protonated di-oxygen species, hydroperoxyl anion (¯OOH), following H2O2-induced metal reduction (Azadmanesh *et al.*, 2025, Azadmanesh *et al.*, 2024).

Overall, we conclude that H_2O_2 treatment does not alter the redox state or coordination geometry of the catalytic Mn in the Gln143Asn enzyme, unlike all other H_2O_2-treated MnSOD variants characterized previously (Azadmanesh *et al.*, 2025, Azadmanesh *et al.*, 2024). This further demonstrates how Gln143Asn is perpetually frozen in the reduced state without the necessary proton transfer events. This loss of redox flexibility at the expense of catalytic turnover distinguishes Gln143Asn from all other spectrally characterized human MnSOD variants to date.

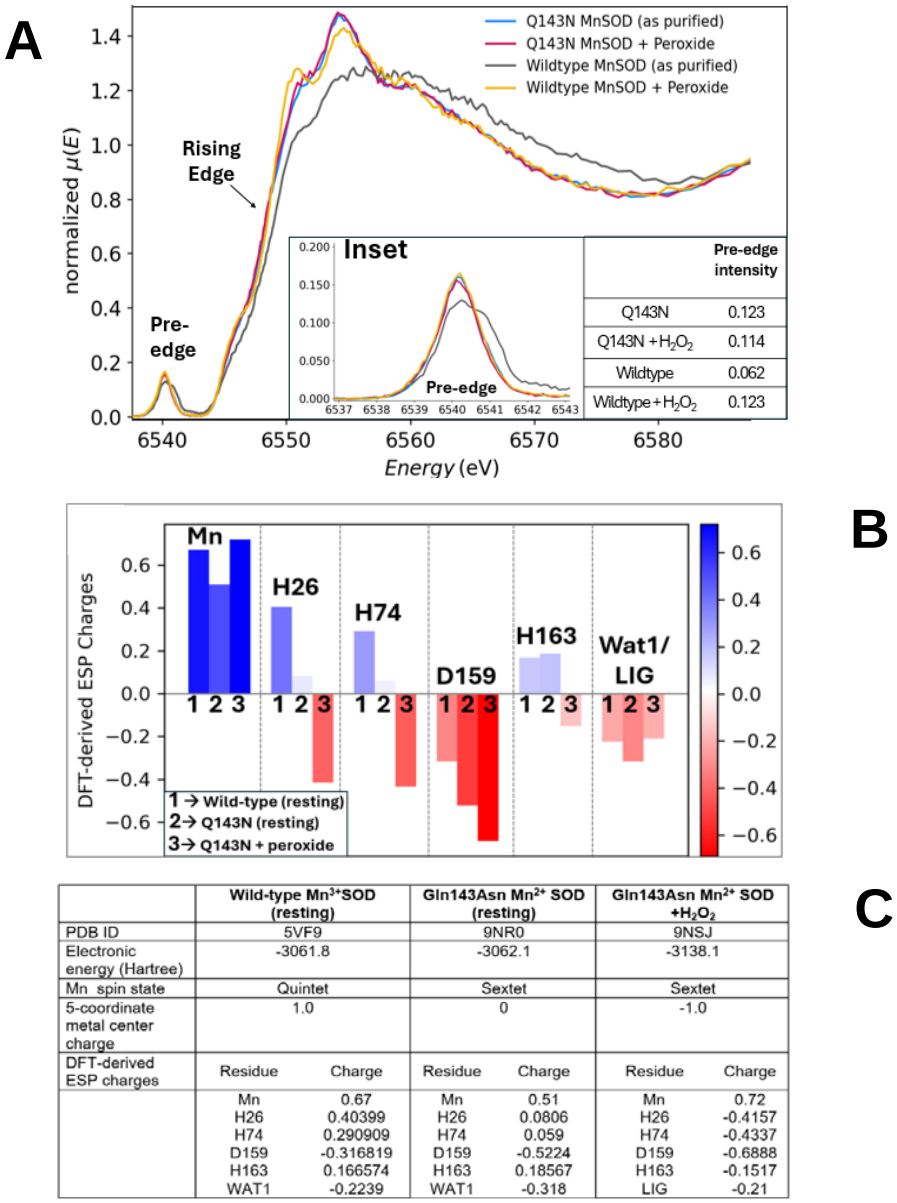

C

	Wild-type Mn^{3+}SOD (resting)		Gln143Asn Mn^{2+} SOD (resting)		Gln143Asn Mn^{2+} SOD $+H_2O_2$	
PDB ID	5VF9		9NR0		9NSJ	
Electronic energy (Hartree)	-3061.8		-3062.1		-3138.1	
Mn spin state	Quintet		Sextet		Sextet	
5-coordinate metal center charge	1.0		0		-1.0	
DFT-derived ESP charges	Residue	Charge	Residue	Charge	Residue	Charge
	Mn	0.67	Mn	0.51	Mn	0.72
	H26	0.40399	H26	0.0806	H26	-0.4157
	H74	0.290909	H74	0.059	H74	-0.4337
	D159	-0.316819	D159	-0.5224	D159	-0.6888
	H163	0.166574	H163	0.18567	H163	-0.1517
	WAT1	-0.2239	WAT1	-0.318	LIG	-0.21

Figure 4 HERFD XANES spectroscopy **(A)** Normalized Mn K-edge HERFD-XANES spectra of wild-type and Gln143Asn MnSOD enzymes, both in resting and H_2O_2-soaked forms. **Inset** shows a magnified view of the pre-edge region (6537–6543 eV), along with their individual pre-edge

intensities. **(B and C)** Mn redox state and/or H_2O_2 treatment affects the individual DFT-derived ESP charges of the Mn primary coordination sphere residues.

4. Conclusions

The high-resolution crystal structure of H2O2-treated human Gln143Asn MnSOD reported herein reveals previously unobserved, L_b H_2O_2 binding sites on the solvent-exposed surface in the bulk solvent, in addition to the canonical LIG and PEO positions (Fig. 2&3). This contrasts with all previously published H_2O_2-soaked MnSOD structures, which have captured H_2O_2 binding only within the first or second coordination shells. Although the fact that product release occurs too rapidly in the wild-type enzyme offers a plausible explanation as to why we do not catch transient H_2O_2 beyond the active site gateway on the solvent-exposed side, their absence even in severely product-inhibited MnSOD variants, such as Trp161Phe and Tyr34Phe, suggests that the principal kinetic bottleneck for product release from MnSOD is H_2O_2 diffusion across the Tyr34-His30 solvent gate. It appears that once beyond this point, H_2O_2 escapes rapidly into bulk solvent, evading experimental detection methods. To overcome this gap, we leveraged the slow kinetics of the catalytically impaired Gln143Asn MnSOD to successfully stabilize several L_b H_2O_2 beyond the active site solvent funnel, thus depicting a more extensive MnSOD H_2O_2-interaction landscape than previously available (Fig. 2). The redox cycling of the active site metal in Gln143Asn MnSOD is impaired, this causes the electrostatic surface to stay in a more neutral condition and the H_2O_2 are fairly immobilized (Supporting Information Fig. S3). These solvent-exposed L_b H_2O_2 likely represent a native ensemble of product molecules diffusing across the active site solvent channel, extending from the gateway at the second shell, to the bulk solvent-exposed surface. This phenomenon has never been structurally visualized before in any H_2O_2-soaked MnSOD enzyme.

Tyr34 in Gln143Asn adopts a dominantly shifted conformation (~80% occupancy), even in the absence of H_2O_2 soaking (Fig. 2D, 3). This conformation is stabilized by an additional solvent molecule position in the mutation-induced cavity, namely, W_{cav}, which in turn orients toward the LIG position-bound species, creating a tight interaction network that could stabilize bound H_2O_2 at the LIG site. This network is not observed in the wild-type or other MnSOD variants, due to steric hindrance from Gln . This water molecule might be able to donate a proton to WAT1, and this may be why Q143N retains some activity. The alternate Tyr34 conformation and the presence of the W_{cav} solvent introduce new hydrogen bonds within the active site of Gln143Asn MnSOD, which are not observed in the wild-type enzyme (Supporting Information Fig. S6). These may contribute to the slightly higher thermal stability of Gln143Asn MnSOD (~1.8 °C) previously reported (Hsieh *et al.*, 1998).

HERFD-XANES and DFT analyses show no detectable change in the oxidation state, coordination number, or spin state of the catalytic Mn^{2+} center of Gln143Asn upon H_2O_2 treatment (Fig. 3A). These results confirm that this MnSOD variant remains stuck in a reduced, catalytically inert state, unable to drive the PCET-mediated MnSOD catalytic cycle. By decoupling proton transfer

from catalysis, the Gln143Asn mutation stabilizes transient H_2O_2-bound states and opens a rare structural window into otherwise elusive steps of MnSOD catalysis. This work underscores the value of catalytically impaired mutants not as dysfunctional models, but as powerful structural probes for revealing elusive mechanistic events in metalloenzymes.

Acknowledgements This research was funded by the NIGMS grant R01-GM145647. The UNMC Structural Biology Core Facility received support from the Fred and Pamela Buffett NCI Cancer Center Support Grant (P30CA036727). The use of the Stanford Synchrotron Radiation Lightsource (SSRL) at SLAC National Accelerator Laboratory, is supported by the US Department of Energy (DOE), Office of Science, Office of Basic Energy Sciences under Contract No. DE-AC02-76SF00515. The SSRL Structural Molecular Biology Program is funded by the DOE Office of Biological and Environmental Research and the NIH National Institute of General Medical Sciences (P30GM133894). The views expressed in this publication are those of the authors and do not necessarily reflect the official positions

References

Abreu, I. A. & Cabelli, D. E. (2010). *Biochim Biophys Acta* **1804**, 263-274.

Azadmanesh, J., Lutz, W. E., Coates, L., Weiss, K. L. & Borgstahl, G. E. O. (2021). *Nat Commun* **12,** 2079.

Azadmanesh, J., Slobodnik, K., Struble, L. R., Lovelace, J. J., Cone, E. A., Dasgupta, M., Lutz, W. E., Kumar, S., Natarajan, A., Coates, L., Weiss, K. L., Myles, D. A. A., Kroll, T. & Borgstahl, G. E. O. (2025). *Nat Commun* **16,** 1887.

Azadmanesh, J., Slobodnik, K., Struble, L. R., Lutz, W. E., Coates, L., Weiss, K. L., Myles, D. A. A., Kroll, T. & Borgstahl, G. E. O. (2024). *Nat Commun* **15**, 5973.

Azadmanesh, J., Trickel, S. R. & Borgstahl, G. E. O. (2017). *J Struct Biol* **199**, 68-75.

Borgstahl, G. E., Parge, H. E., Hickey, M. J., Beyer, W. F., Jr., Hallewell, R. A. & Tainer, J. A. (1992). *Cell* **71,** 107-118.

Bresciani, G., da Cruz, I. B. & Gonzalez-Gallego, J. (2015). *Adv Clin Chem* **68,** 87-130.

Fee, J. A. & Bull, C. (1986). *J Biol Chem* **261**, 13000-13005.

Grujicic, J. & Allen, A. R. (2025). *Antioxidants (Basel)* 1**4**.

Hornak, V., Abel, R., Okur, A., Strockbine, B., Roitberg, A. & Simmerling, C. (2006). *Proteins* **65,** 712-725.

Hsieh, Y., Guan, Y., Tu, C., Bratt, P. J., Angerhofer, A., Lepock, J. R., Hickey, M. J., Tainer, J. A., Nick, H. S. & Silverman, D. N. (1998). *Biochemistry* **37**, 4731-4739.

Hsu, J. L., Hsieh, Y., Tu, C., O'Connor, D., Nick, H. S. & Silverman, D. N. (1996). *J Biol Chem* **271**, 17687-17691.

Liebschner, D. (2020). *Acta Crystallogr D Struct Biol* **76,** 802-804.

Neves, R. P., Sousa, S. F., Fernandes, P. A. & Ramos, M. J. (2013). *J Chem Theory Comput* **9,** 2718-2732.

Olsson, M. H., Sondergaard, C. R., Rostkowski, M. & Jensen, J. H. (2011). *J Chem Theory Comput* **7,** 525-537.

Porta, J., Vahedi-Faridi, A. & Borgstahl, G. E. (2010). *J Mol Biol* **399,** 377-384.

Proux, O., Lahera, E., Del Net, W., Kieffer, I., Rovezzi, M., Testemale, D., Irar, M., Thomas, S., Aguilar-Tapia, A., Bazarkina, E. F., Prat, A., Tella, M., Auffan, M., Rose, J. & Hazemann, J. L. (2017). *J Environ Qual* **46,** 1146-1157.

Reece, S. Y. & Nocera, D. G. (2009). *Annu Rev Biochem* **78,** 673-699.

Van Stappen, C., Deng, Y., Liu, Y., Heidari, H., Wang, J. X., Zhou, Y., Ledray, A. P. & Lu, Y. (2022). *Chem Rev* **122,** 11974-12045.

Supporting information

High-Resolution X-ray Structure of Gln143Asn Manganese Superoxide Dismutase Captures Multiple Hydrogen Peroxide Binding Sites.

Medhanjali Dasgupta,[a] Katelyn Slobodnik,[a] Erika A. Cone,[a] Jahaun Azadmanesh,[a] Thomas Kroll[b] and Gloria E.O. Borgstahl[a*]

[a] Eppley Institute for Research in Cancer and Allied Diseases, University of Nebraska Medical Center, Omaha, NE, 68198, USA

[b] Stanford Synchrotron Radiation Lightsource, SLAC National Accelerator Laboratory, Menlo Park, CA, 94025, USA

[*]Correspondence email*:* gborgstahl@unmc.edu

Table S1 X-ray data collection and refinement statistics.

	Gln143Asn MnSOD (untreated)	**Gln143Asn MnSOD + H_2O_2**
PDB code	9NR0	9NSJ
Resolution range (Å)	37.14 - 1.551 (1.606 - 1.551)	39.34 - 1.33 (1.378 - 1.33)
Space group	P 6_1 2 2	P 6_1 2 2
Unit cell dimensions	78.20, 78.20, 237.21, 90, 90, 120	78.11, 78.11, 236.02, 90, 90, 120
Total no. reflections **No. unique reflections** **No. refinement reflections**	125342 (11951) 62859 (6011) 62854 (6011)	196692 (19149) 98359 (9587) 98339 (9577)
Multiplicity	2.0 (2.0)	2.0 (2.0)
Completeness (%)	99.43 (97.25)	99.89 (99.18)
Mean I/sigma(I)	6.85 (1.02)	9.38 (1.17)
Wilson B-factor	21.12	9.44
R-merge **R-meas**	0.02582 (0.4213) 0.03652 (0.5958)	0.04186 (0.6241) 0.0592 (0.8826)
$CC_{1/2}$	0.999 (0.634)	0.998 (0.541)
R-work	0.1756 (0.3296)	0.1581 (0.3124)
R-free	0.2148 (0.3660)	0.1942 (0.3034)
RMS (bonds) **RMS (angles)**	0.010 0.97	0.012 1.15
Coordinate Error (Å)	0.19	0.15
Ramachandran energetically favored (%)	97.95	97.45
Average B-factor	26.24	16.33
Solvent %	46.94	45.41

Table S2 Active site Mn bond lengths in resting-state and H_2O_2-bound Gln143Asn Mn^{2+} SOD and wildtype Mn^{3+} SOD.

	Gln143Asn Mn^{2+}SOD (resting state) (Å)	**Wt Mn^{2+}SOD (resting state) (PDB 7KLB) (Å)**
PDB ID	9NR0	7KLB
Mn-$N^{\varepsilon 2}$(H26)	2.14 (2.20)	2.18 (2.17)
Mn-$N^{\varepsilon 2}$(H74)	2.12 (2.15)	2.28 (2.16)
Mn-$N^{\varepsilon 2}$(H163)	2.24 (2.16)	2.25 (2.29)
Mn-$O^{\delta 2}$(D159)	2.04 (2.03)	2.09 (2.06)
Mn-O(WAT1)	2.12 (2.10)	2.31 (2.28)
	Gln143Asn Mn^{2+} SOD with H_2O_2 (Å)	**WtMnSOD (PDB 8VJ5) with H_2O_2 (Å)**
PDB ID	9NSJ	8VJ5
Mn-$N^{\varepsilon 2}$(H26)	2.21 (2.18)	2.16 (2.15)
Mn-$N^{\varepsilon 2}$(H74)	2.21 (2.17)	2.18 (2.18)
Mn-$N^{\varepsilon 2}$(H163)	2.18 (2.19)	2.21 (2.24)
Mn-$O^{\delta 2}$(D159)	2.03 (2.03)	2.07 (2.06)
Mn-O(WAT1)	2.16	___
Mn-O_1(Lig)	2.13 (2.09)	2.20 (2.10)
Mn-O_2(Lig)	2.19 (2.20)	2.19 (2.34)

Distances for chain B are in parentheses.

Table S3 Active site water (W_{cav}) coordination in resting-state and H_2O_2-treated Gln143Asn MnSOD.

	Gln143Asn MnSOD untreated (Å)	**Gln143Asn MnSOD with H_2O_2 (Å)**
PDB ID	9NR0	9NSJ
O^H(Y34) - O(W_{cav})	2.01 (2.10)	1.83 (1.94)
$N^{\delta 2}$(N143) - O(W_{cav})	2.79 (2.47)	2.66 (2.52)
O(WAT1) - O(W_{cav})	2.24 (2.35)	2.41

Distances for chain B are in parentheses.

Figure S1 Cryoprotection protocol for Gln143Asn MnSOD crystals: The crystallization drop is shown as a red dashed circle with the final drop volume labeled in blue. The direction of red arrows shows if liquid is pipetted away from the crystal drop, or if cryo-buffer is pipetted into the drop. Only for the H_2O_2-treated Gln143Asn MnSOD dataset, 0.1µL of a 30% stock of H_2O_2 (Sigma Aldrich) was added to a total drop volume of 10 µL to reach a final H_2O_2 concentration of 0.3% in the single crystal (step 11) and allowed to soak for ~30 seconds at room temperature. This was followed by plunging into liquid nitrogen and mounting in the cryostream at SSRL 14-1.

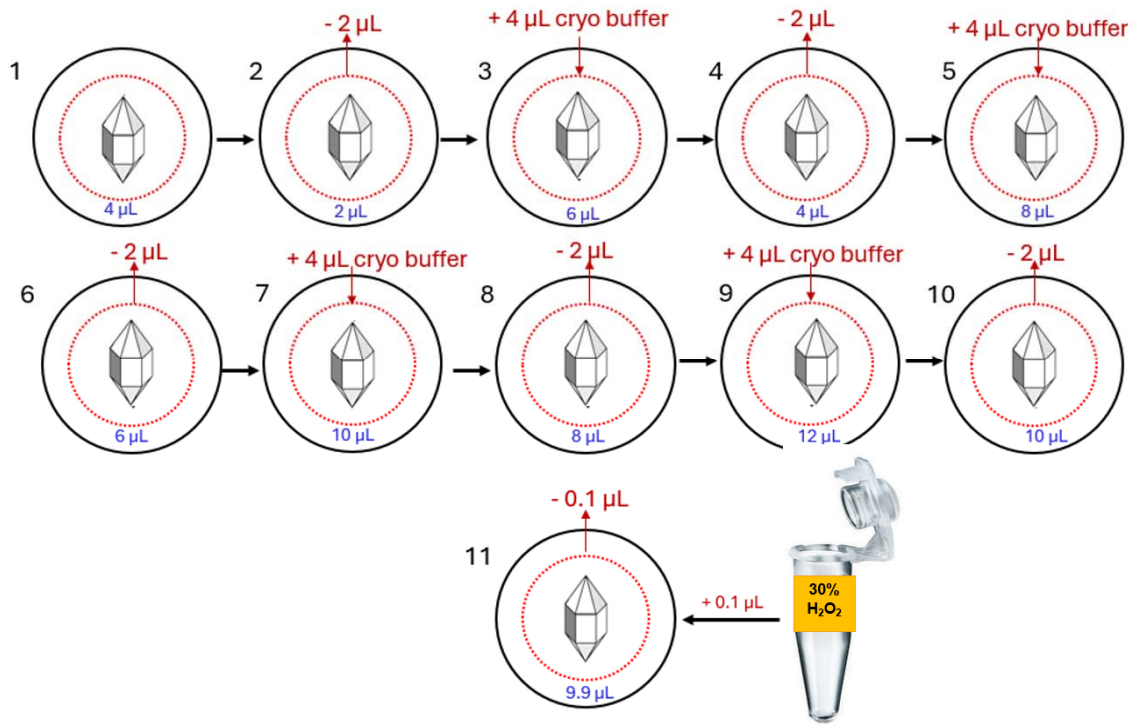

Figure S2 **Workflow for generating metal-centered electrostatic potential maps.**

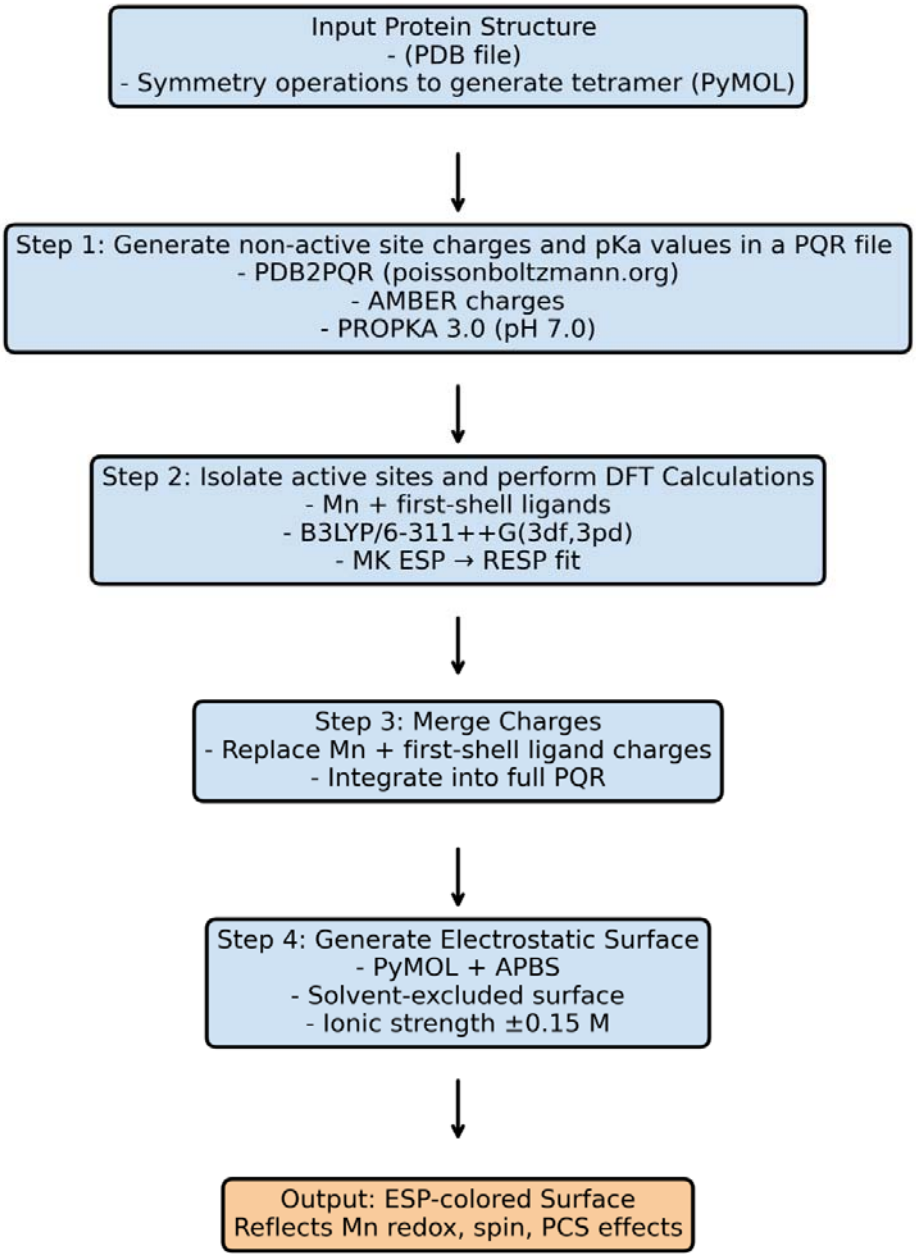

Figure S3 Solvent-exposed bulk peroxide (L_b) modeling trials in Gln143Asn MnSOD.

To rigorously validate the H_2O_2 models, L_b electron densities, a refinement trial was performed where fully occupied water molecule positions from the nontreated, resting-state Gln143Asn MnSOD structure were placed at each L_b sites. 2Fo-Fc electron density maps for modeled L_b H_2O_2 in the H_2O_2-treated structure are shown in blue mesh, and corresponding waters in the resting state structure are a purple mesh. The 2Fo-Fc density is elongated for the L_b sites, and the water are spherical. The Fo-Fc difference densities (green mesh, contoured to 3.0 sigma) in the middle trial panels indicate the need

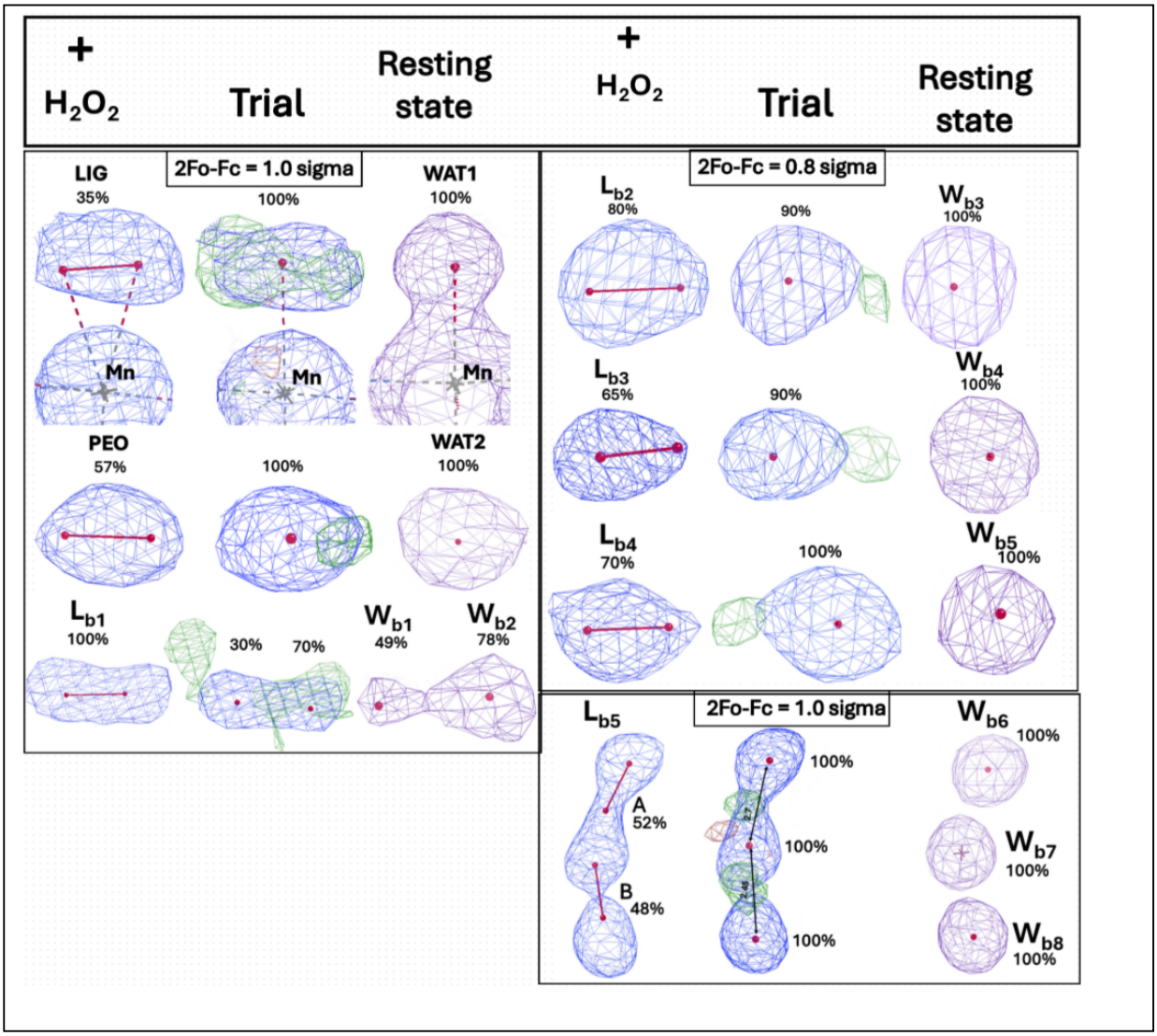

to model two oxygen atoms, rather than one.

Figure S4 The Gln143 to Asn mutation creates a cavity adjacent to the active site which accommodates Tyr34 conformational flexibility in Gln143Asn MnSOD. (A) In the Gln143Asn MnSOD structure, the mutation-induced cavity accommodates a second conformation of Tyr34 (80% occupancy, circled in blue) and an additional water molecule, W_{CAV} (also circled in blue), resulting in new hydrogen bonding interactions. WAT2, located between Tyr34 and His30, is shown as a purple sphere. (B) The same view in reduced wild-type MnSOD (PDB ID: 7KLB) shows no evidence of a second Tyr34 conformation or W_{CAV} and has significantly fewer hydrogen bonds overall. These differences may contribute to the observed ~1.8 °C increase in thermal stability of Gln143Asn MnSOD relative to the wild-type enzyme.

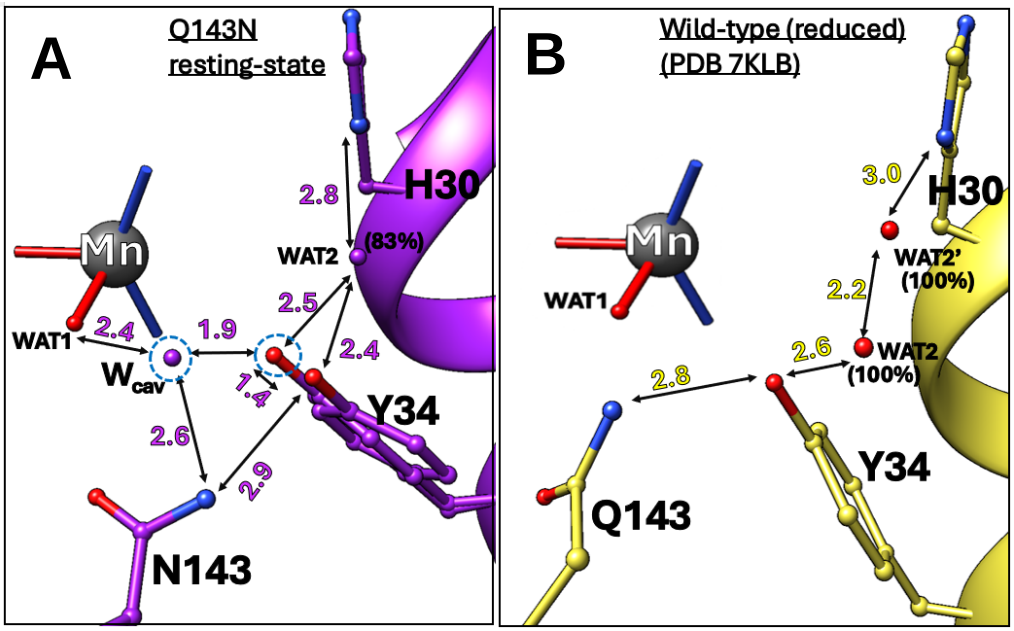

Figure S5 Gln143Asn MnSOD supports a partially hexavalent Mn coordination environment. **(A)** and **(B)** show the resting-state and H_2O_2 -treated active sites of Gln143Asn MnSOD respectively. display significant difference electron densities consistent with the presence of partially occupied sixth ligand (named L_{six}), likely a hydroxide ion (OH^-), opposite Asp159, observed at 23% occupancy in the resting state, and 17% following H_2O_2 exposure. This sixth ligand has previously been reported, only at full occupancy in chain A of the reduced human wild-type Mn^{2+}SOD (PDB 7KKW). Difference densities for the modelled W_{cav} and L_{six} in both structures of the Gln143Asn are represented as mesh, coloured according to their individual contour levels. Presence of this partial sixth coordination partner induces a partial distortion of the Mn^{2+} geometry toward octahedral, diverging from the canonical trigonal bipyramidal configuration characteristic of the penta-coordinate active site

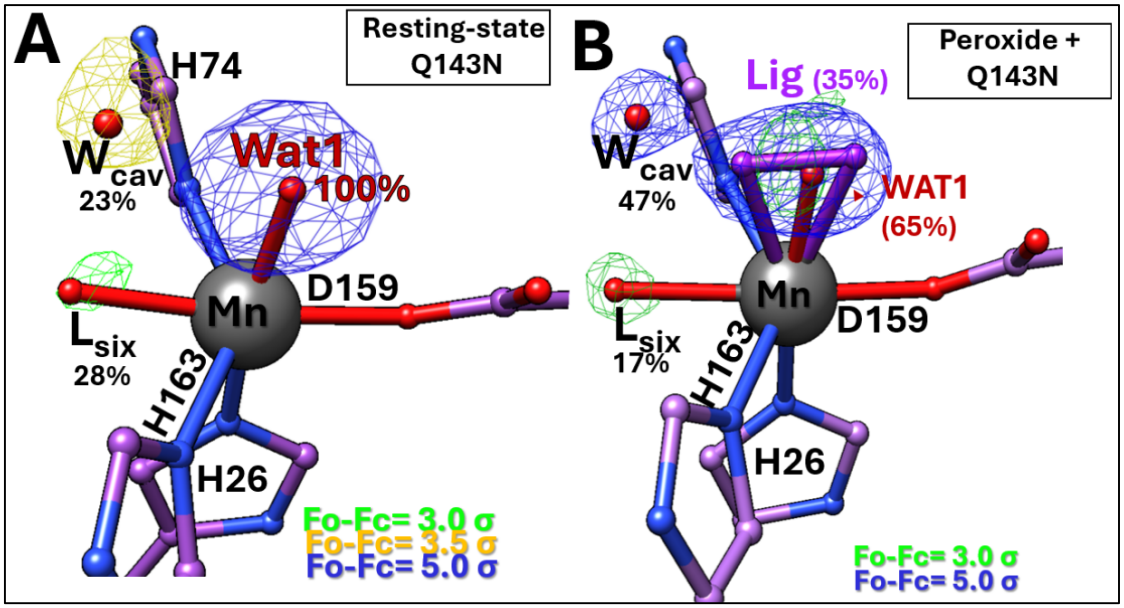

Abreu, I. A. & Cabelli, D. E. (2010). *Biochim Biophys Acta* **1804**, 263-274.

Azadmanesh, J., Lutz, W. E., Coates, L., Weiss, K. L. & Borgstahl, G. E. O. (2021). *Nat Commun* **12**, 2079.

Azadmanesh, J., Slobodnik, K., Struble, L. R., Lovelace, J. J., Cone, E. A., Dasgupta, M., Lutz, W. E., Kumar, S., Natarajan, A., Coates, L., Weiss, K. L., Myles, D. A. A., Kroll, T. & Borgstahl, G. E. O. (2025). *Nat Commun* **16**, 1887.

Azadmanesh, J., Slobodnik, K., Struble, L. R., Lutz, W. E., Coates, L., Weiss, K. L., Myles, D. A. A., Kroll, T. & Borgstahl, G. E. O. (2024). *Nat Commun* **15**, 5973.

Azadmanesh, J., Trickel, S. R. & Borgstahl, G. E. O. (2017). *J Struct Biol* **199**, 68-75.

Borgstahl, G. E., Parge, H. E., Hickey, M. J., Beyer, W. F., Jr., Hallewell, R. A. & Tainer, J. A. (1992). *Cell* **71**, 107-118.

Bresciani, G., da Cruz, I. B. & Gonzalez-Gallego, J. (2015). *Adv Clin Chem* **68**, 87-130.

Fee, J. A. & Bull, C. (1986). *J Biol Chem* **261**, 13000-13005.

Grujicic, J. & Allen, A. R. (2025). *Antioxidants (Basel)* **14**.

Hornak, V., Abel, R., Okur, A., Strockbine, B., Roitberg, A. & Simmerling, C. (2006). *Proteins* **65**, 712-725.

Hsieh, Y., Guan, Y., Tu, C., Bratt, P. J., Angerhofer, A., Lepock, J. R., Hickey, M. J., Tainer, J. A., Nick, H. S. & Silverman, D. N. (1998). *Biochemistry* **37**, 4731-4739.

Hsu, J. L., Hsieh, Y., Tu, C., O'Connor, D., Nick, H. S. & Silverman, D. N. (1996). *J Biol Chem* **271**, 17687-17691.

Liebschner, D. (2020). *Acta Crystallogr D Struct Biol* **76**, 802-804.

Neves, R. P., Sousa, S. F., Fernandes, P. A. & Ramos, M. J. (2013). *J Chem Theory Comput* **9**, 2718-2732.

Olsson, M. H., Sondergaard, C. R., Rostkowski, M. & Jensen, J. H. (2011). *J Chem Theory Comput* **7**, 525-537.

Porta, J., Vahedi-Faridi, A. & Borgstahl, G. E. (2010). *J Mol Biol* **399**, 377-384.

Proux, O., Lahera, E., Del Net, W., Kieffer, I., Rovezzi, M., Testemale, D., Irar, M., Thomas, S., Aguilar-Tapia, A., Bazarkina, E. F., Prat, A., Tella, M., Auffan, M., Rose, J. & Hazemann, J. L. (2017). *J Environ Qual* **46**, 1146-1157.

Reece, S. Y. & Nocera, D. G. (2009). *Annu Rev Biochem* **78**, 673-699.

Van Stappen, C., Deng, Y., Liu, Y., Heidari, H., Wang, J. X., Zhou, Y., Ledray, A. P. & Lu, Y. (2022). *Chem Rev* **122**, 11974-12045.

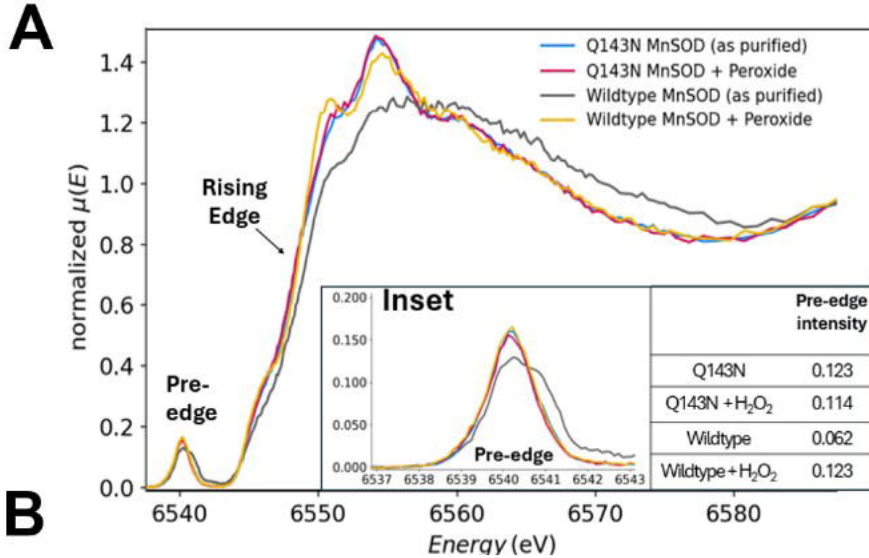

B

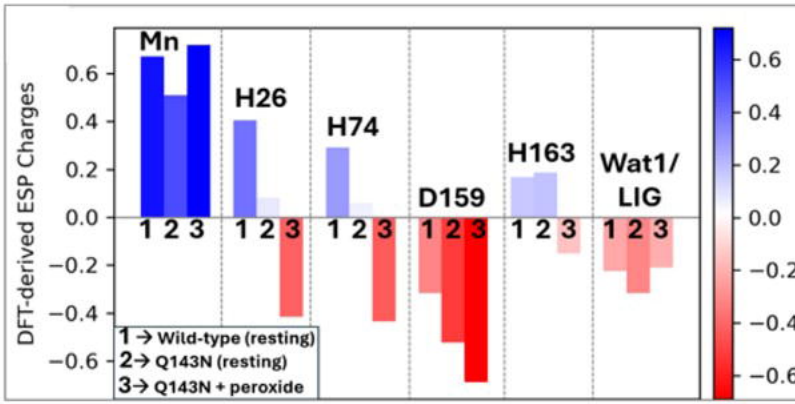

C

	Wild-type Mn^{3+}SOD (resting)		Gln143Asn Mn^{2+} SOD (resting)		Gln143Asn Mn^{2+} SOD $+H_2O_2$	
PDB ID	5VF9		9NR0		9NSJ	
Electronic energy (Hartree)	-3061.8		-3062.1		-3138.1	
Mn spin state	Quintet		Sextet		Sextet	
5-coordinate metal center charge	1.0		0		-1.0	
DFT-derived ESP charges	Residue	Charge	Residue	Charge	Residue	Charge
	Mn	0.67	Mn	0.51	Mn	0.72
	H26	0.40399	H26	0.0806	H26	-0.4157
	H74	0.290909	H74	0.059	H74	-0.4337
	D159	-0.316819	D159	-0.5224	D159	-0.6888
	H163	0.166574	H163	0.18567	H163	-0.1517
	WAT1	-0.2239	WAT1	-0.318	LIG	-0.21

A

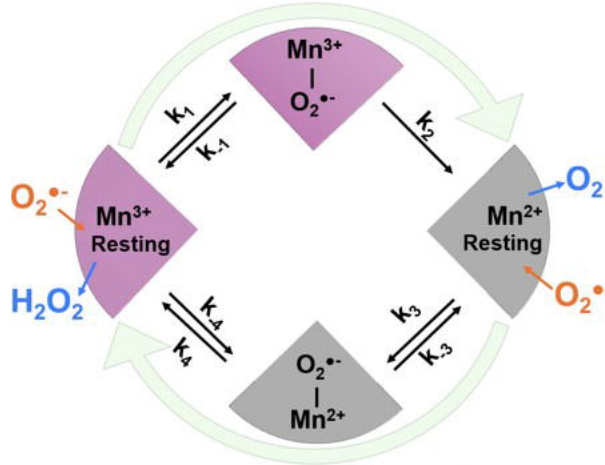

B

Equation	Rate constant	Gln143Asn MnSOD	Wildtype MnSOD
(1) $Mn^{3+} + O_2^{\bullet -} \leftrightarrow Mn^{2+} + O_2$	k_1 ($M^{-1}s^{-1}$)	2.0×10^9	2.0×10^9
	k_{-1} (s^{-1})	1.5×10^6	2.0×10^4
	k_2 (s^{-1})	600	8×10^4
(2) $Mn^{2+} + O_2^{\bullet -} + 2H^+ \leftrightarrow Mn^{3+} + H_2O_2$	k_3 ($M^{-1}s^{-1}$)	2.0×10^9	2.0×10^9
	k_{-3}(s^{-1})	1.5×10^6	2.0×10^4
	k_4 (s^{-1})	600	8×10^4
	k_{-4} ($M^{-1}s^{-1}$)	1×10^3	3×10^2

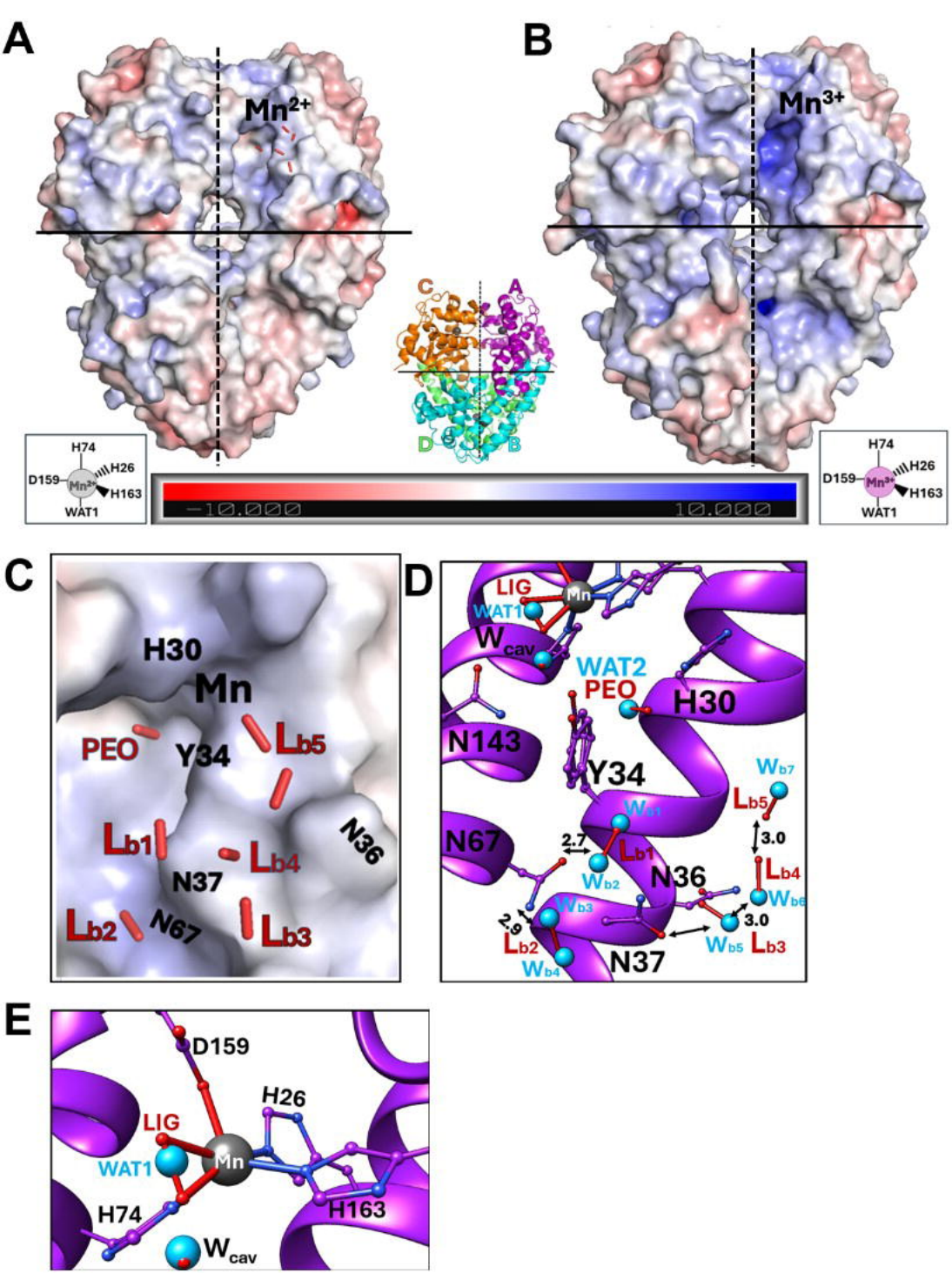
A
Mn2+
B
Mn3+
C
A
D
B
H74
H26
D159
Mn2+
H163
WAT1
−10.000
10.000
H74
H26
D159
Mn3+
H163
WAT1
C
H30
Mn
PEO
Y34
Lb5
Lb1
Lb4
N36
N37
Lb2
N67
Lb3
D
LIG
Mn
WAT1
Wcav
WAT2
PEO
H30
N143
Y34
Wb7
Lb5
Wb1
N67
2.7
Lb1
3.0
Wb2
N36
Lb4
Wb6
Wb3
2.9
3.0
Lb2
Wb5
Lb3
Wb4
N37
E
D159
H26
LIG
WAT1
Mn
H74
H163
Wcav

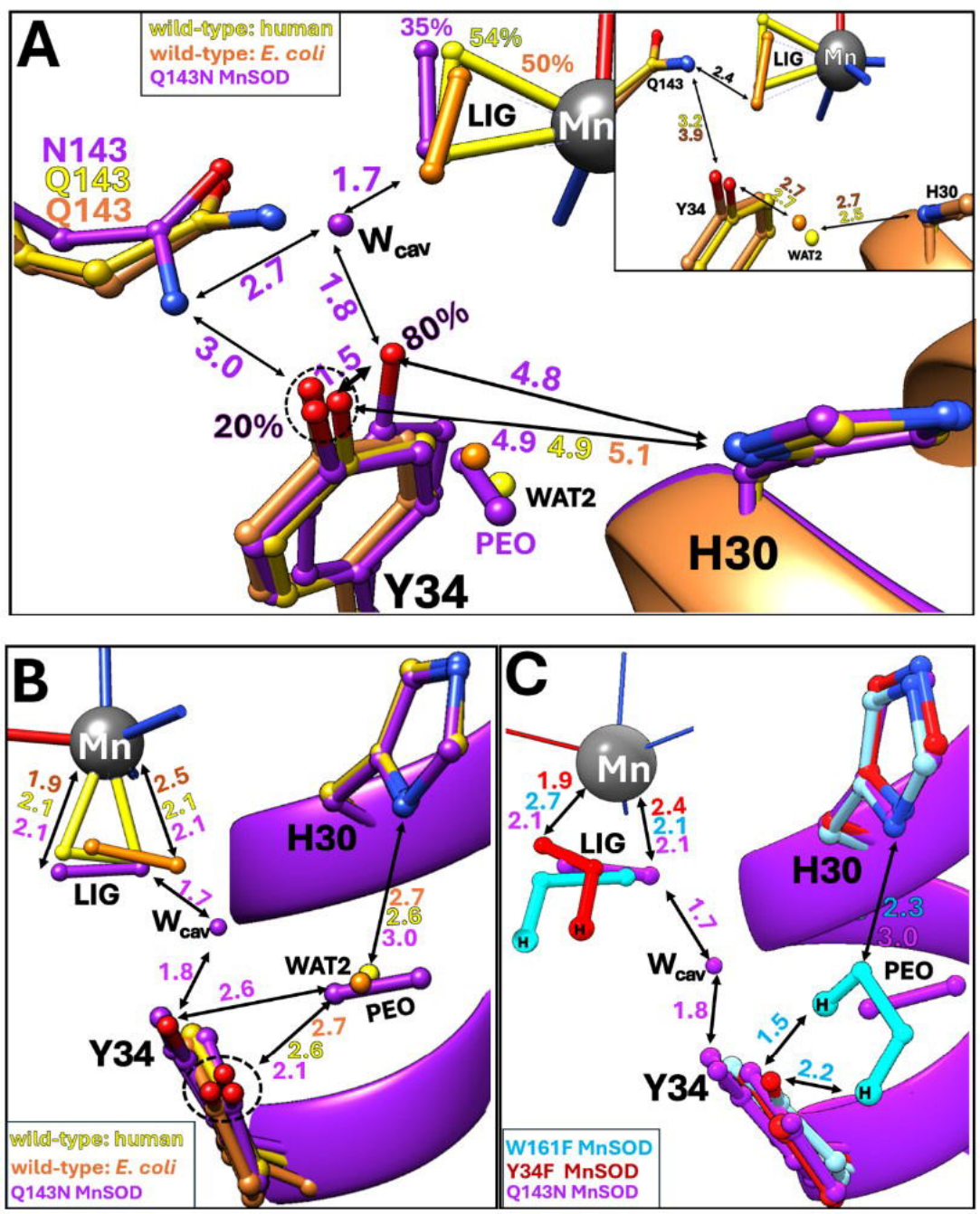
A
wild-type: human
wild-type: E. coli
Q143N MnSOD
35%
54%
50%
LIG
Mn
N143
Q143
Q143
1.7
Wcav
2.7
1.8
3.0
1.5
80%
20%
4.8
4.9
4.9
5.1
WAT2
PEO
H30
Y34
Q143
2.4
LIG
Mn
3.2
3.9
Y34
2.7
3.1
2.7
2.5
H30
WAT2
B
Mn
1.9
2.1
2.1
2.5
2.1
2.1
LIG
1.7
Wcav
H30
2.7
2.6
3.0
1.8
2.6
WAT2
PEO
Y34
2.7
2.6
2.1
wild-type: human
wild-type: E. coli
Q143N MnSOD
C
Mn
1.9
2.7
2.1
2.4
2.1
2.1
LIG
H
H
H30
1.7
Wcav
2.3
3.0
PEO
1.8
1.5
H
Y34
2.2
H
W161F MnSOD
Y34F MnSOD
Q143N MnSOD

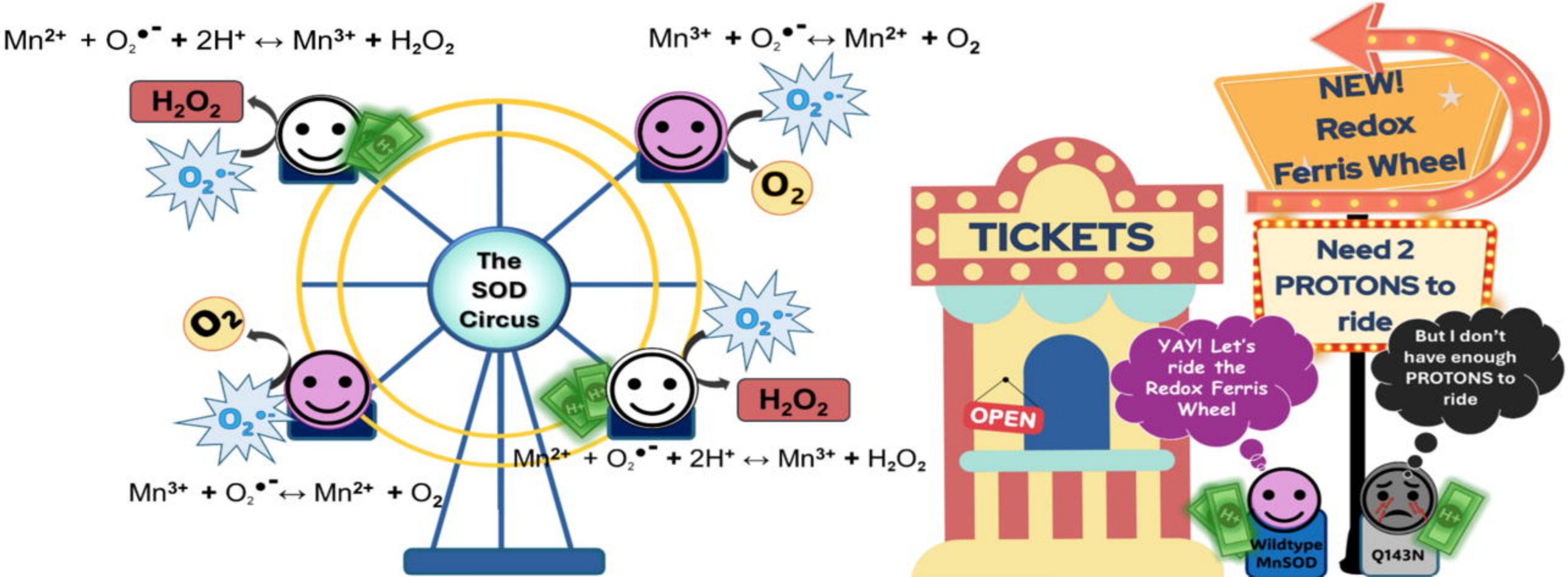
$Mn^{2+} + O_2^{\bullet -} + 2H^+ \leftrightarrow Mn^{3+} + H_2O_2$
$Mn^{3+} + O_2^{\bullet -} \leftrightarrow Mn^{2+} + O_2$
H_2O_2
$O_2^{\bullet -}$
O_2
The SOD Circus
O_2
$O_2^{\bullet -}$
$O_2^{\bullet -}$
H_2O_2
$Mn^{2+} + O_2^{\bullet -} + 2H^+ \leftrightarrow Mn^{3+} + H_2O_2$
$Mn^{3+} + O_2^{\bullet -} \leftrightarrow Mn^{2+} + O_2$
NEW! Redox Ferris Wheel
TICKETS
OPEN
Need 2 PROTONS to ride
YAY! Let's ride the Redox Ferris Wheel
But I don't have enough PROTONS to ride
Wildtype MnSOD
Q143N